Fireside corrosion degradation of 15Mo3, T22, T23 & T91 in simulated coal-biomass co-fired environment

T. Dudziak*, T. Hussain, D. Orlicka, A. Pokrywa and N.J. Simms

This paper reports the result of a fireside corrosion test carried out on four low alloyed ferritic alloys at 650 °C for 1000 h. The combustion gases were derived from co-firing cereal co-product with a UK coal. Synthetic deposits were used to assess the influence of the deposit compositions. The samples were examined using an ESEM/EDX. To quantify the metal damage the pre-exposure micrometre measurements were compared with the post-exposure image analyser measurements on sample cross-sections. The median metal damage of the alloys showed the following ranking (most to the least damage): 15Mo3>T22> T23> T91.

1 Introduction

One of the major issues facing the world is climate change, which is believed to be due to the increase in greenhouse gas emissions. According to the International Energy Agency (IEA) energy statistics, electricity and heat production accounts for 41% of the total CO_2 emission [1–3]. Conventional solid fossil fuel power plants contribute significantly to this CO_2 emission and the EU has put in place legislation to reduce its emission to 20% below the 1990 levels by 2020. The UK also has an ambitious target of reducing CO_2 emissions to 80% of their 1990 levels by 2050 [4]. To meet this ambitious target a combination of renewable fuels such as biomass and highly efficient ultra supercritical power plants with carbon capture and storage technology (CCS) will be necessary.

Biomass co-firing with coal at a lower percentage in conventional pulverised fuel power plants has proved to be a successful way to reduce the overall CO_2 emission from electricity generation industry. Biomass accounts for approximately 70% of total renewable energy production in the world [5]. Biomass absorbs CO_2 during its lifetime and releases the CO_2 during the combustion; hence, it can be classed as carbon neutral. Dedicated biomass fired plants are usually smaller in size (and lower overall efficiency) and the plant can face significant issues with fouling, deposition, agglomeration and corrosion. These issues restrict the overall steam temperature that can be used in those plants. However, burning a smaller percentage of biomass with coal in existing pulverised fuel power plants, which are much larger in capacity and more efficient than dedicated biomass fired plants, can produce more biomass derived renewable energy. Reduction in CO_2 emissions from pulversied coal fired power plants can be achieved by increasing the operating temperature (and pressure) of the steam systems, which results in an increase in overall plant efficiency. Typically 1% increase in absolute efficiency results in as much as 3% reduction in CO_2 emissions [6].

Fireside corrosion has been an on-going concern for the power generation industry where coal has been used as a fuel. Fireside corrosion is defined as the loss of the heat exchanger material due to chemical reactions with the surrounding environment at high temperature. This can lead to tube failures, which are expensive to repair and unplanned shutdown which can cause large financial losses. In addition, future ultra-supercritical/supercritical plants will operate at steam temperatures beyond 700 °C to increase the overall efficiency in power generation [3]. Increased operating temperatures coupled with biomass derived fuel gases will exacerbate the fireside corrosion problem. Typically, the fireside corrosion shows characteristic bell-shaped curves, where the corrosion rate increases with increasing temperature and then decreases as the deposit becomes unstable. It has been reported that the peak corrosion damage in air-fired combustion gases occurs around 650 °C [7–9]. Therefore, it is important to investigate the fireside corrosion performance of the ferritic alloys at that temperature. Assuming the fireside corrosion mechanism operating in the temperature ranges 550– 650 °C remain the same, increasing the temperature would also accelerate the corrosion rates which will provide valuable information about

T. Dudziak
Foundry Research Institute in Cracow, Zakopiańska 73 30–418, Kraków (Poland)
E-mail: tomasz.dudziak@iod.krakow.pl

T. Hussain
Division of Materials, Mechanics and Structure, University of Nottingham, Nottingham, NG7 2RD (UK)

D. Orlicka, A. Pokrywa, N.J. Simms
Institute of Energy and Resource Technology, Cranfield University, Cranfield, MK43 0AL (UK)

This study has been performed in Cranfield University at Institute of Energy and Resource Technology, MK43 0AL, (UK).

the lifetime of the heat exchanger materials. Furthermore, it is important to investigate the influence of various chemical compositions in the deposit on the fireside corrosion mechanisms.

Therefore this paper reports the results of the influence of different chemical compositions of the deposits on the ferritic steels in simulated fireside corrosion tests. The laboratory tests were conducted with 15Mo3, T22, T23 and T91 materials in simulated air-fired combustion gases at metal temperature higher than average conventional operating temperatures of the existing pulverised fuel power plants. The gas and deposits were selected based on co-firing a UK coal with a cereal co-product (CCP).

The performance of the alloys was investigated with five different deposits. The work was carried out according the "deposit-recoat" test method that has been developed for high temperature corrosion tests and was used in recent years [8,10]. Dimensional metrology has been used as the primary route to quantify the metal damage occurring due to fireside corrosion. The exposed samples were examined in environmental scanning electron microscope (ESEM) in backscattered electron mode (BSE) equipped with energy dispersive X-ray spectrometry (EDX) to characterise corrosion degradation.

2 Experimental procedure

2.1 Materials

In this study four alloys were used: a low carbon ferritic steel with no Cr (15Mo3), two ferritic steels with 2.3 wt.% Cr (T22 and T23), and one ferritic/martensitic steel with 9 wt.% of Cr (T91). The materials were chosen to investigate the mechanism under different deposits in air-fired conditions. The materials represent materials currently used for the superheater/reheater tubes (SH/RH) in pulverised fuel power plants. The nominal chemical compositions of the materials are shown in Table 1. Each of these materials was machined from commercial boiler tubes of various dimensions. The shape of the samples used in this study is shown in Figure 1. 15Mo3 was machined as rectangular section (due to lack of tube segments) and the rest of the materials were machined as tube segments. The typical dimensions of specimens were ~ 15 mm long, ~10 mm wide/chord (for tube sections) with a 4 mm wall thickness. All surfaces of these tubes were machined to a UK 600 grit surface finish (Ra <0.4 μm).

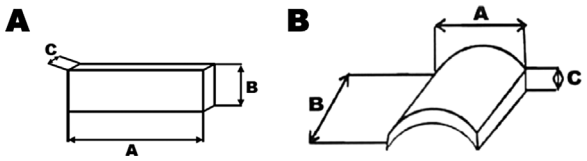

Figure 1. Geometry of the exposed materials: A) 15Mo3, B) T22, T23 and T91

2.2 Gases and deposits

The exposure conditions were determined following a detailed investigation of the gaseous environments and deposit conditions that could be found around heat exchangers (superheaters/reheaters) in conventional pulverised fuel power plants using a UK daw mill CCP [7,10,11] as mentioned previously in this study.

The co-firing ratio of the biomass was 20 wt.% for this study, the compositions of the fuels are available in ref. [7]. The gas composition from the combustion of these fuels were calculated using pre-existing models and simplified to their active components for corrosion testing in the controlled atmosphere furnaces. The nominal gas compositions used in the corrosion tests are shown in Table 2.

The alloys were exposed with five synthetic deposits in this test programme. Table 3 shows the composition of the deposits. The deposits in the experiment were chosen to simulate the deposits formed on the heat-exchanger surfaces in the pulverised fuel power plants. In this study in total 24 samples were used, 4 samples without deposit (D0) and another 20 specimens with 5 different deposits (D1–D5). The deposits can be characterised as follows:

D0: no deposit (i.e., bare alloy surface exposed to the gas atmosphere).

D1: a standard deposit composition that is widely used in screening tests; it represents a composition of alkali iron tri-sulphate that has been identified from many investigations as the principal cause of fireside corrosion in superheaters/reheaters in coal-fired power stations [9,11,12].

D2: the alkali iron tri-sulphate compositions from D1 diluted with kaolinite ($Al_2O_3.2SiO_2.2H_2O$) to represent the clay minerals usually found in coals along with Fe_2O_3 and CaO. K_2SO_4 concentration was decreased to 0%, whereas Na_2SO_4 was reduced to 10% in order to minimise aggressiveness of the deposit D2.

D3: is similar to D2 but with equal amount of K_2SO_4 and Na_2SO_4 (5%) to increase the aggressiveness of the deposit, other

Table 1. Nominal compositions (wt.%) of the materials used in the fireside corrosion test.

Alloy	Fe	C	Mn	P	S	Si	Cr	Ni	Mo	V	W	Nb	B	Al	N	Cu
15Mo3	Bal	0.16	0.65	0.035	0.035	0.35	-	-	0.30	-	-	-	-			-
T22	Bal.	0.10	0.5	0.025	0.025	0.50	2.30	-	1.00	-	-	-	-			-
T23	Bal	0.06	0.46	0.001	0.014	0.20	2.18	0.14	0.08	0.25	1.54	0.05	0.0023	0.001	0.0023	-
T91	Bal	0.10	0.45	0.003	0.009	0.12	8.36	0.21	0.90	-	-	-	-	0.022	0.48	0.17

Table 2. Nominal composition of the mixture of gases when used in the corrosion test

O_2 %	CO_2 %	H_2O %	N_2 %	SO_2 vpm	HCl vpm
4	13.4	8.6	Bal.	1300	400

elements (kaolinite, Fe_2O_3 and CaO) are in the same concentration as shown in D2.

D4: is similar to D3, but with more KCl (10%) to investigate the sensitivity of the corrosion damage as a result of biomass co-firing. D4 does not contain any K_2SO_4; however Na_2SO_4, Fe_2O_3 and CaO phases are in the same amounts as in D3.

D5: is similar to D2, with the same amount of Na_2SO_4 (10%). Hematite (Fe_2O_3) concentration in both deposits is the same; however, D5 does not contain any CaO (burnt lime).

2.3 Experiment setup

The fireside corrosion exposures were carried out in an alumina lined vertical controlled-atmosphere furnace using simulated air-fired combustion gases. A schematic diagram of the fireside corrosion tests is shown in Figure 2.

The furnace accommodates 24 test pieces in alumina crucibles at one time in the hot zone. Each test was run for 1000 h using the widely accepted "deposit-recoat" method [8]. Prior to sample exposure, the samples were cleaned using a degreaser (volasil) followed by isopropanol in an ultrasonic bath at a temperature of 35 °C for 20 minutes. For those samples being exposed with a surface deposit, the cleaned samples were painted using a paintbrush to apply a deposit loading of ~20 mg/cm^2. The test was cycled every 200 h and fresh deposits were applied on the exposed samples in order to replenish the salts resulting in a deposition flux of 100 μg/cm^2/h (no deposit was removed before painting in this widely accepted deposit-recoat test method). As part of the deposit-recoat process (5 cycles), the samples were weighed every 200 h with and without crucibles as well as before and after applying the deposits.

Premixed gases were supplied to the controlled-atmosphere furnace through mass flow controllers to achieve the desired gas composition. The gas containing (CO_2, O_2, N_2) was passed through a de-ionized water bubbler, which was kept at 40 °C in a water bath to add the required amount of moisture to the gas stream (8.6 vol.%) before mixing with the corrosive species (HCl, SO_2).

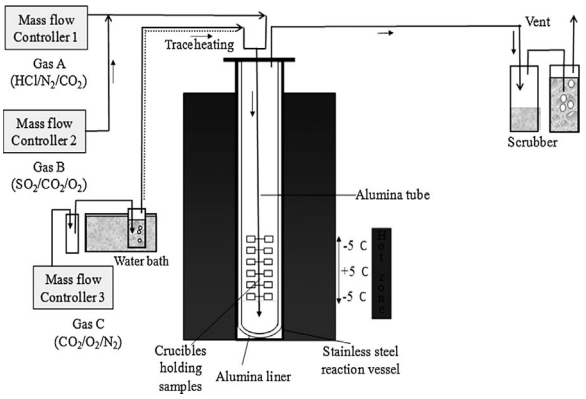

Figure 2. A schematic diagram of the fireside corrosion test setup

2.4 Sample metrology: pre- and post-exposure measurements

Following the exposures, the samples were vacuum mounted using a low shrinkage cold mounting resin filled with ballotini (to further reduce shrinkage) in a bespoke jig. The mounted sample was cross-sectioned, ground and polished to 1 μm using non-aqueous lubricant. ESEM fitted with an EDX system was used to investigate the scale/deposit thickness and microstructure.

The dimensional metrology of the samples is a key feature of this test programme. The dimensions of each sample were measured before the exposure using a micrometre (with resolution of 1 μm). Post-exposure measurements were carried out using a LEITZ WEIZLAR optical microscope coupled to an IMAS image analysis system with a calibrated x-y stage capable of positioning the sample to an accuracy of ± 2 μm. The system can automatically take groups of pictures from locations evenly spaced around the sample outer edge. From these pictures, positions of the outer sample surface, and depth of internal damage are determined (using x-y coordinates of the features of interest relative to a reference point for whole sample). By comparing sample dimensions before and after exposure, the apparent metal

Table 3. Deposits used in the simulated air-fired experiments (mol%)

Deposit	Kaolonite	Fe_2O_3	CaO	$CaCO_3$	Na_2SO_4	K_2SO_4	KCl
D0	0	0	0	0	0	0	0
D1	0	25	0	0	37.5	37.5	0
D2	57	28	5	0	10	0	0
D3	57	28	5	0	5	5	0
D4	53	27	5	0	5	0	10
D5	57	28	0	5	10	0	0

loss and the change in sound metal (metal loss + internal damage) can be calculated.

These data sets can then be re-ordered (from greatest to least metal loss) and corrected for calibration differences (using data from reference samples). The processed data can then be plotted as a metal loss vs. cumulative-probability. This measurement method was performed in accordance with the draft standard methods for high temperature corrosion assessment [11].

3 Results

3.1 Kinetics

Mass change data is the most conventional and frequently reported method of observing metal oxidation and corrosion at high temperatures. Figures 3–8 illustrate the specific net mass change [mg/cm^2] vs. time [h] of the exposed samples: 15Mo3, T22, T23 and T91 with deposits D0–D5 after 1000 h of exposure at 650 °C. 15Mo3 shown in Figure 3 showed the highest mass gain when bare alloy was exposed and the lowest rate of corrosion was observed in T91 where concentration of Cr was the highest. The alloys T22 and T23 (with similar Cr content) showed similar kinetic behaviour.

It is difficult to rationalise the mass change data of the alloys with deposits in high temperature fireside corrosion. Nonetheless, the mass change data for the alloys under all five deposits are presented in this paper for comparative purposes. Figure 4 shows mass gain of all alloys used in this study under D1 deposit. The results show much higher mass gain under deposit D1 than under other deposits used in this work. Ferritic alloys under D1 deposit could not form a protective oxide scale to improve its corrosion behaviour. Kinetic behaviour showed linear characteristics, where mainly chemical reactions at the deposit/oxide scale interface and the oxide scale/substrate interface determined the performance. The highest mass gain was seen by T22 alloy, the lowest mass gain was seen by T91 alloy. Such behaviour indicates the amount of Cr in the alloy did not correlate to their performance under the aggressive deposit.

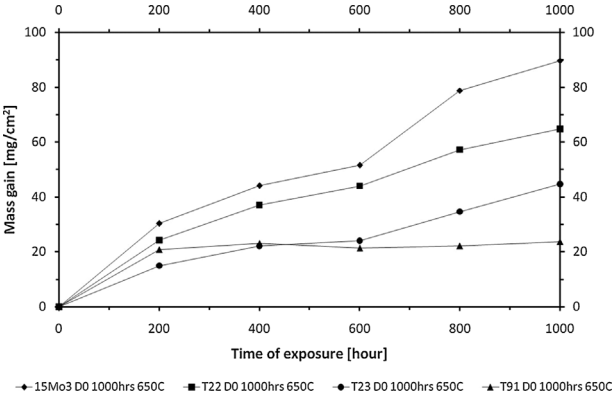

Figure 3. Mass gain of the alloys exposed with no deposit (D0) at 650 °C in air-fired conditions

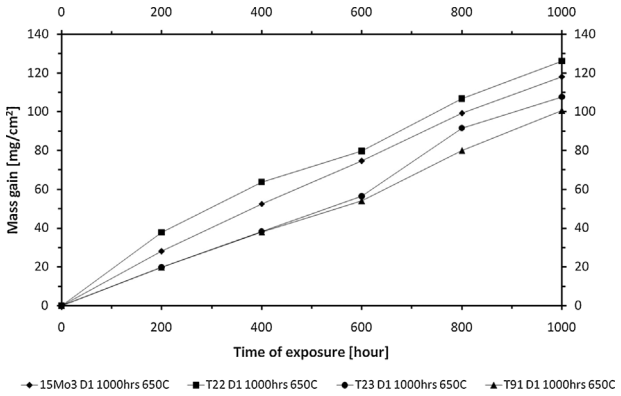

Figure 4. Mass gain of the alloys exposed with D1 deposit at 650 °C in air-fired conditions

There was no clear distinction in the mass gain data of the alloys under deposits D2, D3, D4 and D5 shown in Figures 5–8 respectively. The alloys covered by the deposits D2–D5 were rich in kaolinite (alumina silicate found in coal ash) and much lower corrosion degradation was observed compared to deposit D1. Typically, the lowest corrosion rate was found in T91 alloy which contains 9 wt.% of Cr and the highest in 15Mo3.

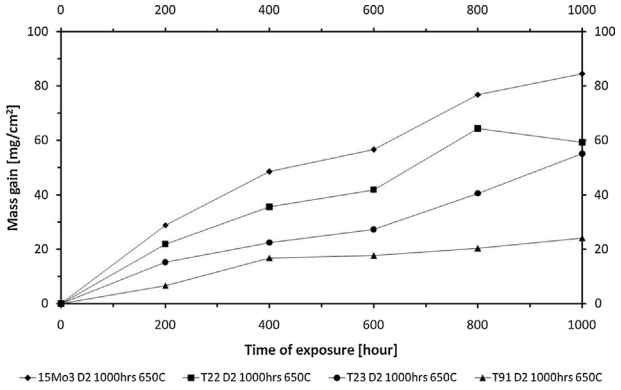

Figure 5. Mass gain of the alloys exposed with D2 deposit at 650 °C in air-fired conditions

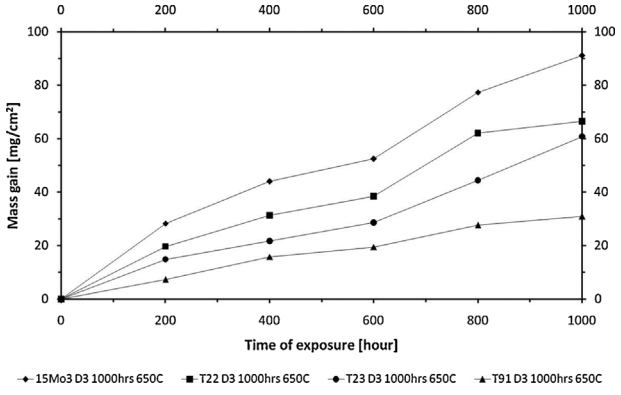

Figure 6. Mass gain of the alloys exposed with D3 deposit at 650 °C in air-fired conditions

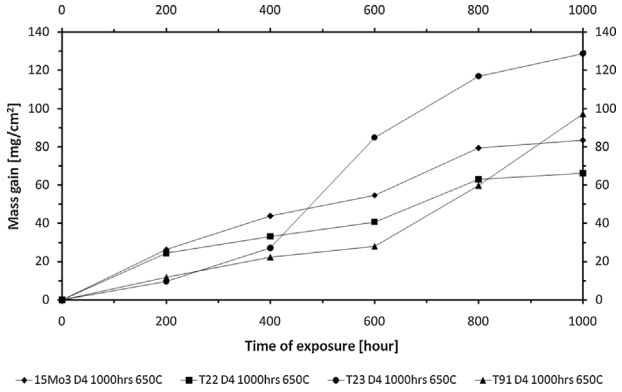

Figure 7. Mass gain of the alloys exposed with D4 deposit at 650 °C in air-fired conditions

3.2 Microstructural investigations

The surface observations were conducted only for the alloys with no deposits; however, due to the similarity in microstructures micrographs are not shown here. Alloy 15Mo3 showed needle like structure growing uniformly across the surface, which suggests a highly active surface going through rapid oxidation/corrosion degradation. The oxide growing on the T22 alloy was not uniform and had several bald patches. In contrast, the surface of the T23 did not show the needle like structure. The alloy with the highest Cr content (T91) showed irregular oxide growth similar to the T22; however the shapes of the oxides were well defined. It can be concluded that all four materials underwent corrosion degradation in the simulated co-fired combustion gases without any deposit.

In general, porous and non-protective scales developed on the surfaces of the exposed alloys. The analyses performed by EDX confirmed that mainly Fe_2O_3, Fe_3O_4 and some amounts of sulphur was found in the interface oxide scale/substrate. The higher amount of Cr did not result in a non-porous and uniform oxide growth on the surface. The samples were cross-sectioned to identify the composition of the mixed oxides-corrosion products.

The cross-sectioned microstructural analysis was performed on the materials with deposit D1 (most aggressive) and without deposit D0 (no deposit) only in order to study the scale/corrosion product morphology and degradation after exposure. The alloys with deposit D2–D5 were as well investigated using SEM/EDX and optical microscope; however, these observations are not shown here. The purpose of this work was to focus on the most corroded samples and the samples with no deposit in order to compare and evaluate corrosion rate to establish a rank order of alloys.

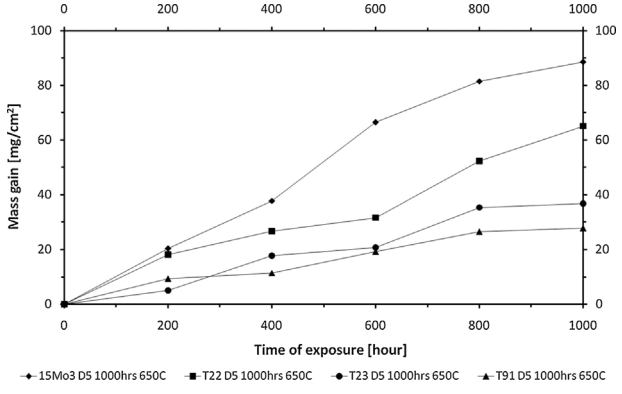

Figure 8. Mass gain of the alloys exposed with D5 deposit at 650 °C in air-fired conditions

Figures 9A – 9D show the cross–sectioned images of all four exposed materials after 1000 h in simulated co-fired combustion gases with no deposit (D0). The BSE images indicate that all four materials underwent a high degree of corrosion as expected. Thick (~500 µm) layer of oxide scale was formed on 15Mo3, which delaminated from the substrate (either during sample preparation or thermal cycling). The oxide scale consisted of Fe_2O_3 (top layer ~150 µm) and inner part was occupied exclusively by Fe_3O_4 with additional amounts of sulphur (up to 1.8 wt.%), thickness of the scale reached ~350 µm. The scale consisted of trace amount of Mn at the oxide scale-substrate interface.The oxide scale on T23 did not show any lateral cracks like the scale grown on the T22. However, the scale on the T22 showed higher surface roughness (Ra) at the scale-metal interface. The scale grown on the T23 is a multi-layered structure slightly enriched in the interface by Cr and W diffused from the bulk alloy. The lack of adherence could be enhanced by thermal stresses within the oxide scale upon heating and cooling. The alloy with the highest Cr content (T91) showed very thin oxide scale formation (~100 µm); however, this oxide scale detached from the substrate either due to the high stress concentration level upon cooling or during sample preparation.

Figures 10 and 11 show phase stability diagrams for Fe–S–O and Cr-S-O respectively in air fired conditions. The stability phase diagrams were calculated using FACTSAGE software [13]. The stability phase diagrams show that Fe_2O_3 and Fe_3O_4 are stable under air-fired conditions. The test condition used in this study is also identified in the figure. At the higher partial pressure of SO_2, FeS and FeS_2 phases are thermodynamically stable. Cr-S-O phase diagram indicates formation of Cr_2S_3 at high partial pressure of SO_2 and a low partial pressure of O_2, which could form only at the interface of oxide scale and the substrate. This phase could form only in the alloy with the highest Cr content (T91) where activity of Cr enhances the formation of Cr_2S_3. Cr_2O_3 is stable over a large range of partial pressure of O_2.

Figures 12A – 12D show the cross section images of 15Mo3, T22, T23 and T91 after 1000 h exposure with a screening deposit D1 (Na_2SO_4 37.5 mol.%, K_2SO_4 37.5 mol.%, Fe_2O_3 25 mol.%). All the four alloys showed similar scale morphologies under D1 deposit. It was found that Cr level did not play an important role in the corrosion protection of the alloys when covered with D1 deposit. The level of Cr in the alloys could not form a protective oxide layer under the test conditions with such an aggressive deposit. The exposed samples underwent high degradation rate, where thick non-protective scales formed. Na, S and K from D1 deposit diffused towards the oxide scale interface and Cr diffused outwards from the exposed alloys to form the oxide scales.

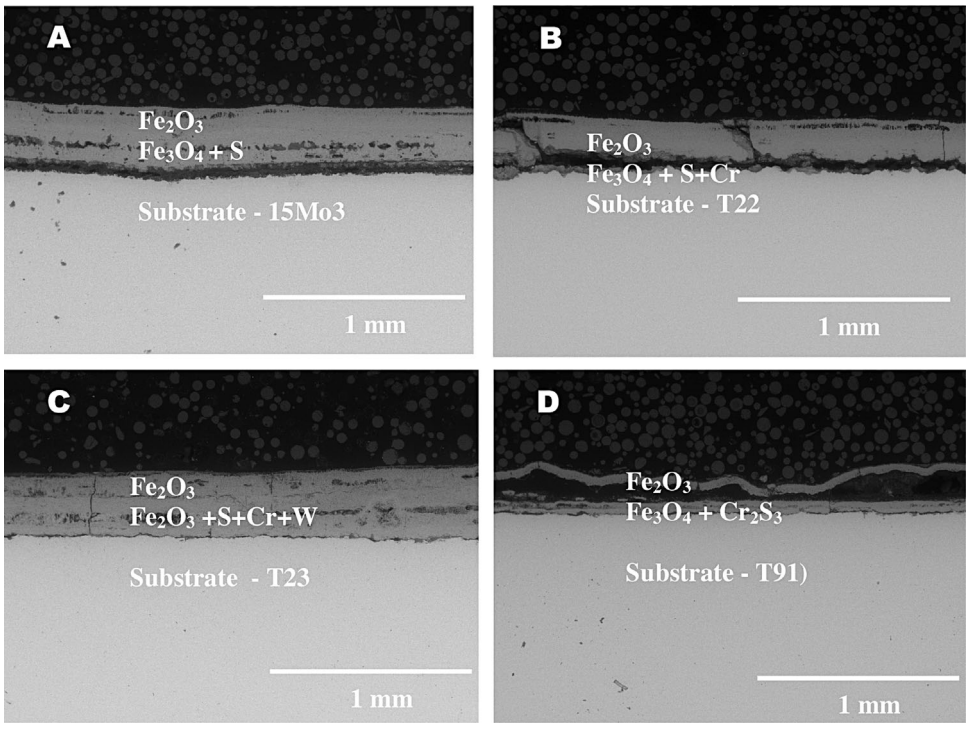

Figure 9. Cross sectioned images in the BSE mode of: A) 15Mo3, B) T22, C) T23 and D) T91 alloys exposed in air-fired condition at 650 °C for 1000 hours without deposit (Do)

Morphologically, the oxide scales are very similar despite different Cr content in the base alloys - the alloys mainly developed Fe_3O_4. Fe_2O_3 was not found within the oxide scale but a small amount of Fe_2O_3 phase was found in mixed deposit scale.

3.3 Metal loss data of the exposed materials

Dimensional metrology provides the most reliable measurement of the corrosion damage to the alloys in fireside corrosion. It produces a distribution of metal damage data for each exposed sample. The results are plotted as "metal loss" vs. "cumulative probability" according to the draft standard for high temperature corrosion measurements [8,11]. Figures 13A – 13D show the metal loss data of all the four exposed materials at 650 °C after 1000 h of exposure in air-fired conditions with all deposits (D0-D5).

The alloys cover with deposit D1 showed the highest corrosion degradation in all four alloys. A useful way of comparing the data is to look at the median (50% cumulative probability) metal loss. For example, Figure 13 shows that the median metal loss of 15Mo3 was ~580 µm with deposit D1 and

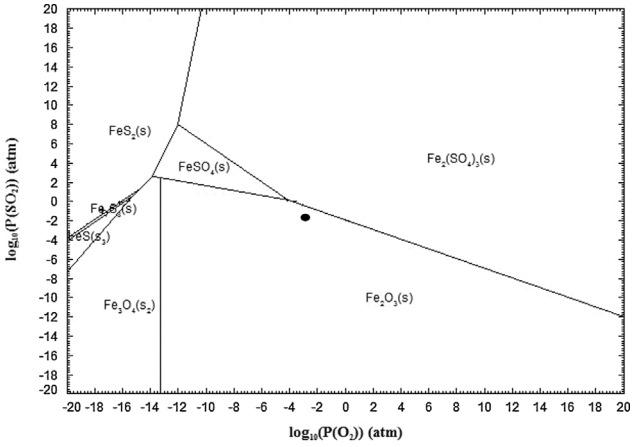

Figure 10. Phase stability diagram for Fe-S-O in air fired conditions at 650 °C; black dot represents an indication of experiment conditions in partial pressure of SO_2 and O_2

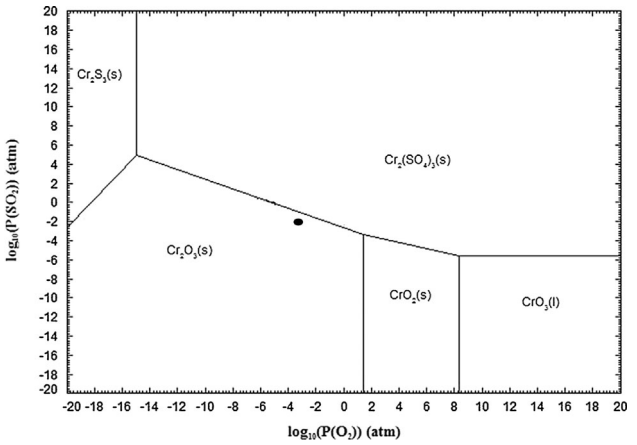

Figure 11. Phase stability diagram for Cr–S–O in air fired conditions at 650 °C; black dot represents an indication of experiment conditions in partial pressure of SO2 and O2

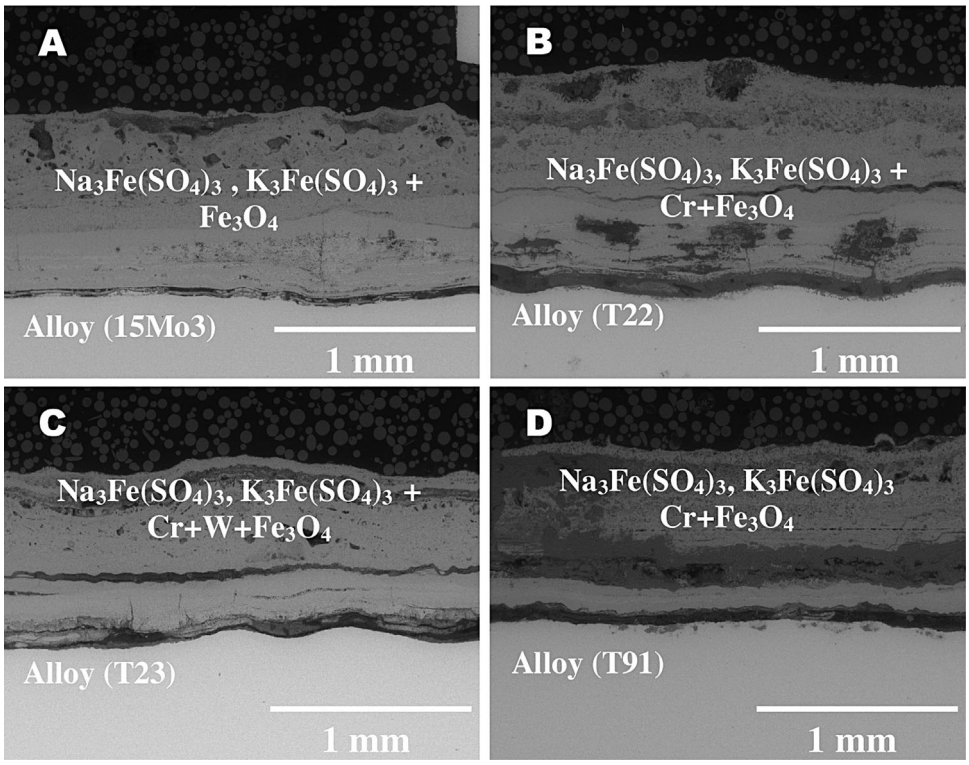

Figure 12. Cross sectioned images in the BSE mode of: A) 15Mo3, B) T22, C) T23 and D)T91 alloys exposed in air-fired condition at 650 °C for 1000 hours with deposit 1 (D1)

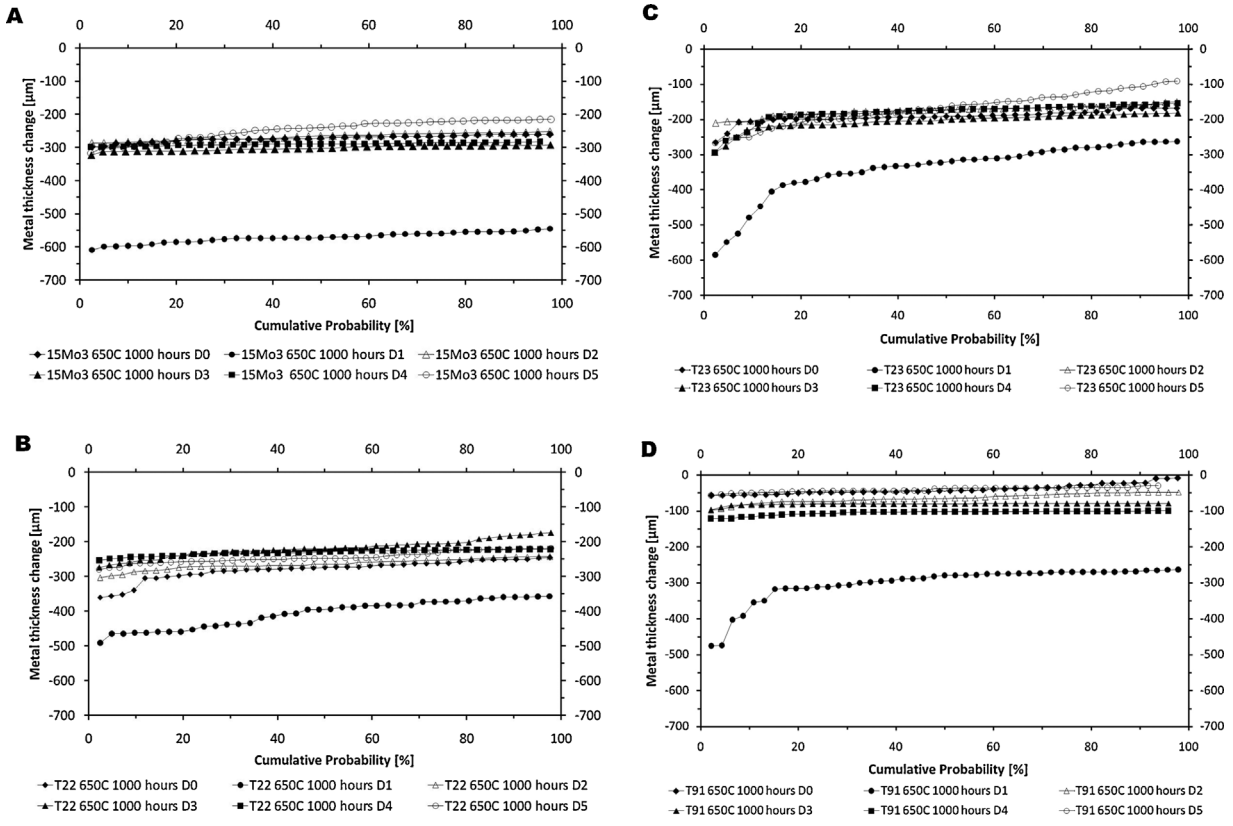

Figure 13. Change in metal thickness versus cumulative probability showing the fireside corrosion behaviour of: A) 15Mo3, B) T22, C) T23 and D) T91 alloys in this test with Do–D5 deposits for 1000 hours at 650 °C

$\sim$ 300 µm with the rest of the deposits. The rates are excessive compared to the traditional target corrosion rate value for superheater/reheater materials in conventional power plants, which is around 40–50 µm/1000 h. It should be noted that deposit D1 is an aggressive deposit mainly used for screening tests. Corrosion degradation of all the four alloys using deposit D0, D2- D5 were mostly uniform as can be seen from the lack of a step change in the cumulative probability curves. However, this was not the case with the T23 and T91 alloys exposed with deposit D1. Figures 13 C- D show that ~18% of the T23 sample surface suffered from a corrosion damage in excess of ~400 µm and similarly ~16% of the T91 sample surface suffered from a corrosion damage in excess of ~280 µm with deposit D1. This is due to the formation of localised pits on the sample surface.

A strong relationship between the corrosion degradation with the Cr content of the alloy was observed in the dimensional metal loss data. The lowest degradation was seen in T91 and the highest degradation was seen in 15Mo3 (looking at the median metal damage). The median metal loss vs. Cr content of the alloys (increasing order) with all the deposits are shown in Figure 14. The metal loss values have been multiplied by −1 and presented as metal loss in this figure. The figure shows that the median metal loss values decreased with increasing the Cr content of the alloy; for example with deposit D1 the following median metal loss values were observed: ~570 µm in 15Mo3, ~400 µm in T22, ~320 µm in T23 and ~ 280 µm in T91. It is worth pointing out that T23 outperformed T22 in these test conditions. Both T22 and T23 contain similar amount of Cr but T22 contains 1% Mo and T23 contains 1.5% W and no Mo.

4 Discussion

Discussion in this work is divided into subsections; subsection 4.1 is focussed on the alloys exposed to fireside corrosion regime with no deposit, subsection 4.2 describes the corrosion mechanisms induced by deposit D1, subsection 4.3 discusses the role and mechanism under deposit D2, subsection 4.4 focuses on deposit D3, subsection 4.5 discusses the role of deposit D4, finally subsection 4.6 shows outlook on deposit D5.

4.1 Alloys with no deposit

The study showed that ferritic steels 15Mo3, T22 and T23 exposed to fireside conditions without deposit generally developed thick and non-protective scales. Lack of adherence between the layers in the formed oxide scale in ferritic steels with low amount of Cr can be attributed to the unbalanced fluxes across the scale and unbalanced diffusional processes known as Kirkendall effect [14].

The morphology in 15Mo3 alloy developed the scale consisting Fe_2O_3 (top layer) and Fe_3O_4 (inner layer) only with additional amount of sulphur (1.7 wt.%). Ferritic steel with 2.3 wt.% of Cr showed better morphology than that observed in 15Mo3, the oxide scale more adherent where no spallation or detachment was observed. The scale consisted of Fe_2O_3 at the top and Fe_3O_4 in the middle part of the oxide scale with small amounts of sulphur 0.5 wt.% and chromium 2.5 wt.% at the interface. The oxide scale formed on T23 alloy showed similar phase composition where top layer was composed of Fe_2O_3 and inner layer was composed of Fe_3O_4 with up to 2.5 wt.% of

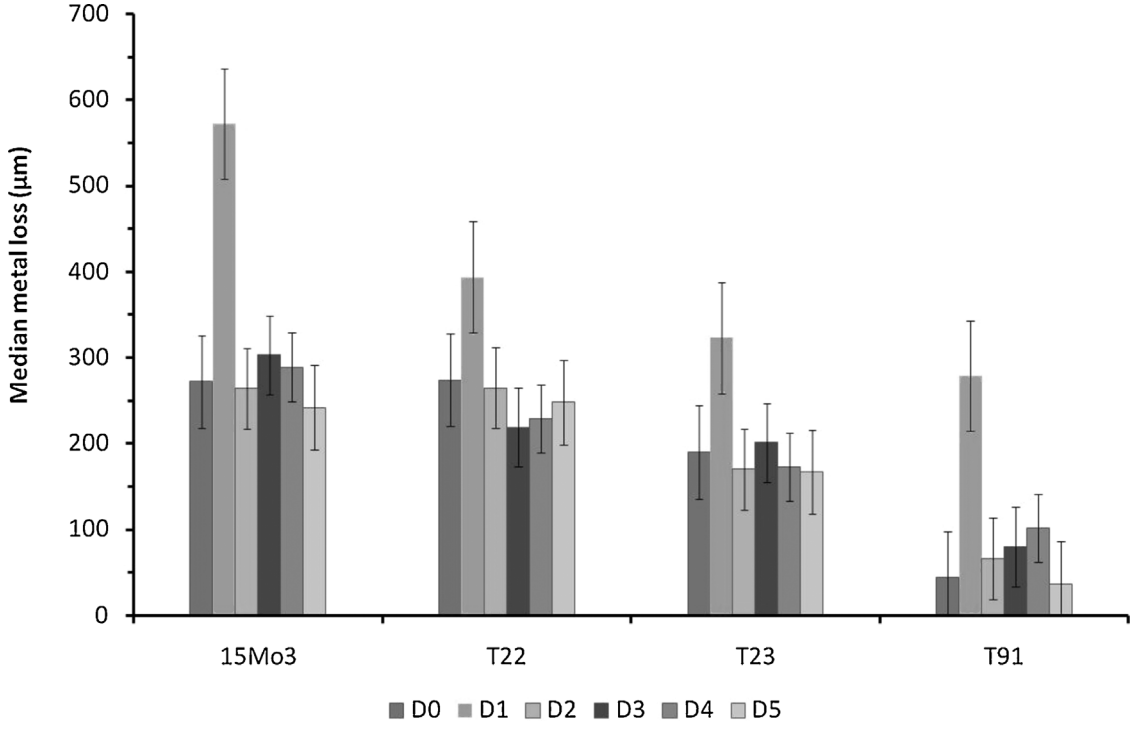

Figure 14. Median change in metal loss of 15Mo3, T22, T23 and T91 alloys after 1000 h at 650 °C in simulated co-fired combustion gases with deposits (Do-D5)

sulphur, chromium (2.8 wt.%) and tungsten (2.6 wt.%). It is believed that W is added to T23 in order to support Cr diffusion to the oxide scale during the high temperature exposure. The mechanism can be explained through the chemical reaction where C from the alloy forms WC carbide and further formation of carbide decreases the activity of both C and W thus Cr activity can be increased.

$$W + C \rightarrow WC \quad (1)$$

The addition of W to T23 alloy should enhance the activity of Cr to form more protective scale than that formed in T22 alloy where Cr from the bulk alloy is directly consumed for the reaction with C in order to form carbides such as Cr_3C_2, Cr_7C_3, and $Cr_{23}C_6$ [15], which decreases the Cr activity resulting in formation of thicker non protective scales. Nevertheless, both low-alloyed steels T22 and T23 formed thick scales in this study.

T91 alloy with the highest Cr content, showed the formation of thin non adherent oxide scale with following phases: top layer was occupied by Fe_2O_3, inner layer was occupied by Fe_3O_4, the inner most layer was occupied by Cr_2S_3. The layer of Cr_2S_3 according to *Huczkowski* et al. [16] formed due to the inward diffusion of SO_2 from ambient atmosphere through the porous oxide scale. The formation of Cr_2S_3 is due to the very low partial pressure of oxygen and high partial pressure of sulphur. Thus in such conditions, it is more likely to form Cr_2S_3 than Cr_2O_3. The high activity of Fe driven by high concentration and inward diffusion of sulphur from ambient atmosphere can form Fe-S phase; however, Cr_2S_3 is more stable and the level of sulphur within the oxide scale decreases constantly, thus FeS formation is not favourable. In contrast to *Huczkowski* et al. [16], *Stringer* et al. [17] concluded that patches of FeS can be observed in the deep regions in the interface of the oxide scale and ash deposit.

4.2 Alloys with D1 deposit

All four alloys formed thick 1 mm scales, suggesting significant corrosion damage under aggressive deposit D1 (Figure 12). It is believed that observed degradation was due to the formation of alkali iron tri-sulphates, which was detected in XRD scans on the surface of the samples following exposure [18]. Chemical composition of the deposit D1 used in this work was designed to invoke the formation of alkali iron tri-sulphates [8,12] and the EDX analyses of the exposed samples following exposure also showed compositions similar to alkali iron tri-sulphates [10,19] [20]. Moreover, alkali iron tri-sulphates were reported in other studies where deposit composition similar to the composition of D1 was used [20].

According to *Natesan* et al. [9] and later *Karlsson* et al. [21] corrosion induced by alkali iron tri-sulphates begins from the formation of thin layer on the metal surface, or by the oxidation of Fe-S phase in coal to form iron oxide in SO_2/SO_3 gases. Alkali sulphates with oxides of sulphur in the boiler are deposited over the oxide scale on the exposed materials.The outer surface of the deposit due to temperature gradient becomes sticky and particles of ash are captured. Increasing temperature of the deposit induces thermal dissociation of sulphur compounds in the ash and releases SO_3, which diffuses to the cooler part of the material, while a layer of the slag forms on the outer surface. The chemical reaction of the formation of alkali iron tri-sulphates occurs through the following way [9]:

$$SO_{2(g)} + \frac{1}{2}O_{2\,(g)} \rightarrow SO_{3(g)} \quad (2)$$

$$Fe_2O_{3(s)} + 3SO_{3(g)} \rightarrow Fe_2(SO_4)_{3\,(s)} \quad (3)$$

$$3(Na/K)_2SO_{4(l)} + Fe_2(SO_4)_{3(s)} \rightarrow 2(Na/K)_3Fe(SO_4)_{3(s,l)} \quad (4)$$

Corrosion degradation increases with increasing temperature in the presence of molten deposits, below 428 °C corrosion rate in low ferritic steels is very low (1.5 mm per year), at 539 °C corrosion rate increases two orders of magnitude (350 mm per year) and 3000 mm per year corrosion rate is observed when temperature reaches melting point of alkali iron tri-sulphates at around 638–677 °C [22]. The temperature depends on the chemical compositions and SO_2/SO_3 balance in the atmosphere [23,24]. Corrosion rate decreases as the deposit becomes unstable due to a shift in the balance of SO_2/SO_3 towards SO_2 at higher temperatures. The formation of unstable (in this conditions) $Fe_2(SO_4)_3$ reacts further with Na and K to form alkali iron tri-sulphates.

4.3 Alloys with D2

Deposit D2 contained much lower concentration of sodium and potassium sulphate than that observed in deposit D1 and similar amounts of hematite. Reduced amounts of sulphates were replaced by kaolinite in order to reduce aggressivess of the deposit. The results achieved in this study clearly show that lower corrosion degradation was observed. It is believed, that lower corrosion rate was reduced by addition of kaolinite to the deposit D2. Addition of kaolinite reduced concentration of sodium and potassium sulphates, as a result much lower corrosion degradation was observed. The addition of CaO (burnt lime) combined with $Al_2O_3.2SiO_2.2H_2O$ (kaolinite) resulted in reduction of active alkali flux in the deposit. At high temperatures kaolinite underwent series of transformations. Endothermic dehydration reaction due to the large amount of energy required to remove the chemically bonded hydroxy ions starts at temperature range 550–600 °C. As a result, kaolinite dehydration of kaolinite produces disordered meta kaolinite $Al_2Si_2O_7$ according to the following reaction [25]:

$$2Al_2SiO_5(OH)_{4\,(s)} \rightarrow 2Al_2Si_2O_{7\,(s)} + 2H_2O_{(g)} \quad (5)$$

The addition of CaO (burnt lime) in D2 does not play an important role due to the low concentration; however, 5% of CaO represents characteristic value for the fly ash derived from coal burning process. CaO plays an important role in slagging and deposit formation, where very high fusion temperatures tend to inhibit the eutectic effect of alkalis. Reducing sodium

sulphate concentration in D2 compared to deposit D1 decreased the rate of corrosion degradation where much lower mass gain was observed. There were no potassium species present in the deposit D2 and hence only sodium iron tri-sulphate was formed exclusively according to the reactions (2) – (4). The formation of alkali iron tri-sulphate was described in reaction (4), alkali iron tri-sulphate formed beneath the layers of sticky ash where oxygen partial pressure was much lower than sulphur.

4.4 Alloys with deposit D3

The alloys covered with deposit D3 underwent similar corrosion rate as those covered by D2, however chemistry of D3 was slightly different than observed in D2. Deposit D3 contained 5% of K_2SO_4 where in D2 deposit K_2SO_4 was not present. Presence of K_2SO_4 should increase corrosion degradation of low alloyed steels, however as the study showed kinetics and metal loss were similar to those obtained under D2 deposit. The exposure of the low alloyed steels invoke several reactions at high temperature. Firstly, at high temperature the alloys formed the scale consisted of Fe_3O_4 (inner layer) and Fe_2O_3 (top layer), further, deposit D3 started to react with the formed oxide scale with gaseous elements such as HCl to form MCl, where M (K, Na or Fe). *Aho* et al. [26] proposed the following mechanism:

$$2MCl + SO_{2(g)} + \frac{1}{2}O_{2\,(g)} + H_2O_{(g)} \rightarrow M_2SO_4 + HCl \quad (6)$$

$$Al_2O_3 \cdot SiO_2 + 2MCl + H_2O \rightarrow M_2O + Al_2O_3 \cdot SiO_2 + 2HCl \quad (7)$$

Further, *Aho* et al. [26] concluded that depending on the initial concentration of alkali, sulphur, kaolinite, chlorine co-combustion favoured the inhibition of chlorine deposition especially by the mechanism shown above. This mechanism can be confirmed in this study as well,

In spite of the addition of 5 wt.% K_2SO_4 in D3 did not change the overall degradation mode. Moreover, it can be assumed that the high concentration of kaolinite and CaO acted as a buffer. The following reactions can take place during high temperature exposure in air-fired conditions. The formed oxide scale consisting mainly Fe_3O_4 reacts with K_2SO_4 and Na_2SO_4 similar to reaction (4), whereas kaolinite decompose to meta kaolinite according to reaction (5) shown previously. At the same time, CaO can react with K_2SO_4 and form calcium sulphate and potassium oxide respectively:

$$K_2SO_{4\,(s)} + CaO_{(s)} \rightarrow Ca(SO_4)_{(s)} + K_2O \quad (8)$$

Further $CaSO_4$ reacts with both sulphates Na_2SO_4 and K_2SO_4 according to the following reaction:

$$2CaSO_{4(s)} + K_2SO_{4(s)} \rightarrow K_2Ca_2(SO_4)_{3(s)} \quad (9)$$

$$2CaSO_{4(s)} + Na_2SO_{4(s)} \rightarrow Na_2Ca_2(SO_4)_{3(s)} \quad (10)$$

Kinetic data and metal loss data obtained in this work clearly shows that both sodium and potassium calcium tri-sulphate $Na_2Ca_2(SO_4)_3$ and $K_2Ca_2(SO_4)_3$ respectively are far less corrosive than $K_3Fe(SO_4)_3$ and $Na_3Fe(SO_4)_3$ formed under deposit D1.

The bio fuels with high annual growth, such as fast-growing woods, forest residues, annual crops and straws, all have abundant alkali in the ash where potassium, in particular volatilizes and reacts readily during combustion. Wood fuels contain approximately 0.1% elemental potassium (K) compared with 1% or higher in straws and grasses, hulls, pits and shells [27].

4.5 Alloys with deposit D4

Deposit D4 was introduced in this study in order to investigate the sensitivity of corrosion damage as a result of biomass co-firing. Thus the mechanism of corrosion under D4 deposit can be explained in the following way: the alloy with low concentration of Cr in the matrix is unable to form a protective oxide scale and thus undergoes corrosion degradation according to chlorine mechanism, where firstly HCl (400 ppm) decomposes at high temperature to H_2 and Cl_2:

$$HCl \rightarrow H_{2\,(g)} + Cl_{2\,(g)} \quad (11)$$

Due to the decomposition of HCl concentration of both hydrogen and chlorine increase. Hydrogen can cause hydrogen embrittlement of the oxide scale [20,21] whereas chlorine further accelerates degradation rate of the low-alloyed steels by means of chlorine effect. According to *Nieken* et al. [28] mechanism can be rationalized by the Deacon reaction:

$$HCl + \frac{1}{2}O_2 \rightarrow Cl_{2\,(g)} + H_2O_{(g)} \quad (12)$$

The reaction can be further accelerated by the oxidised surface. According to the thermodynamics of the Metal-Cl-O system, metal oxides are stable at high oxygen partial pressures while metal chlorides can be expected in regions with low oxygen partial pressure. Thus, such conditions are expected at the surface of the oxide scale where oxygen partial pressure is higher than that observed underneath deposit. The metal chlorides are usually observed at the metal-scale interface (low pO_2), while the outer part of the scale (high pO_2) contains mainly metal oxides [29,30]. It is also known that chlorine diffuses inwards through the oxide scale of Fe_3O_4. At the metal/oxide interface the oxygen pressure is low and metal chlorides are stabilised according to the following reaction:

$$Me_x + \frac{1}{2}Cl_2 \rightarrow MeCl_{x\,(s,g)} \quad (13)$$

The vapour pressure of the chlorides at elevated temperature reach significant values and volatile chlorides diffuse towards oxygen rich outer part (oxide scale) where it undergoes destabilisation [29,30].

$$2MeCl_2 + \frac{3}{2}O_2 \rightarrow Me_2O_{3(s)} + 2Cl_{2\,(g)} \quad (14)$$

Due to the formation, decomposition reaction in this model, oxide scale formed on low-alloyed steels frequently detached from the metallic core and spallation is observed. Besides, the chlorine model shown above the material exposed in this study suffered from the formation of alkali iron tri-sulphates, however with much lower aggressiveness as was observed under deposit D1. Potassium chloride at high temperatures undergoes decomposition to free potassium and chlorine and these elements react directly with the formed oxide scales; in low-alloyed steels with Fe_3O_4 (chlorine cycle), whereas in the alloy with higher Cr content reaction can lead to the formation of chromates:

$$KCl_{(s)} + Cr_2O_{3\,(s)} + H_2O_{(g)} + \frac{3}{4}O_2 \rightarrow K_2CrO_4 + 2HCl_{(g)} \quad (15)$$

The formation of stable chromates compounds decreases the total concentration of Cr in the oxide scale leading to the formation of much poorer scales with lower corrosion resistance due to lower Cr content.

4.6 Alloys with deposit D5

Chemically deposit D5 showed similar composition to D2, D3 and D4, where high content of Al_2O_3 and SiO_2 with 10% of Na_2SO_4 and lack of K_2SO_4. Deposit D5 contained $CaCO_3$ instead of CaO presented in D4. The corrosion degradation rate under deposit D5 was similar to deposits under D2–D4 based on kinetic and metal loss data.. Similar to other deposits high temperature such as 550–600 °C invoked dehydration of kaolinite producing disordered meta kaolinite $Al_2Si_2O_7$ [25]. The addition of $CaCO_3$ combined with $Al_2O_3.2SiO_2.2H_2O$ led to reduction of active alkali flux in the deposit based on the results achieved in this work.

It needs to be pointed out, that $CaCO_3$ (limestone) in presence of SO_2 (flue gas at high concentration) forming calcium sulphate and carbon dioxide according to the following reaction:

$$CaCO_{3\,(s)} + SO_{2\,(g)} + \frac{1}{2}O_{2(g)} \rightarrow CaSO_{4\,(s)} + CO_{2\,(g)} \quad (16)$$

Comparable to D3 deposit, in D5 deposit $CaSO_4$ reacts with sodium sulphate (Na_2SO_4) as shown below:

$$2CaSO_{4(s)} + Na_2SO_{4(s)} \rightarrow Na_2Ca_2(SO_4)_{3(s)} \quad (17)$$

The sodium calcium tri-sulphate $Na_2Ca_2(SO_4)_3$ based on kinetics and the metal loss data is less corrosive than $K_3Fe(SO_4)_3$ and $Na_3Fe(SO_4)_3$ formed under deposit D1. Furthermore, much lower mass gain of the low-alloyed steels was found because of the high concentration of kaolinite added to decrease corrosive behaviour of 10% of Na_2SO_4 in D5 deposit [10].

5 Conclusions

The aim of this study was to investigate the corrosion behaviour of four ferritic alloys: 15Mo3, T22, T23 and T91 in simulated co-fired combustion gases for 1000 h at 650 °C with different chemistry of the deposits. Dimensional metrology was used as the primary route to quantify the material damage and to produce statistically significant metal loss distributions. The cross-sections of the samples were examined in ESEM/ EDX.

The following conclusions can be made from this study:

1. The materials covered with deposit D1 showed the highest specific net mass gain and the highest metal loss due to the formation of alkali iron tri-sulphates. The alloys covered in deposit D1 underwent high corrosion rate due to the lack of formation of a protective oxide layer.
2. The alloys formed non-protective oxide scales consisting of Fe_2O_3 (top layer) and Fe_3O_4 (inner layer) when no deposit was used (deposit D0). Additional elements such as S and Cr were detected in the scales formed on T22; S, Cr and W in T23 and Cr_2S_3 in T91. Thick scales were formed on 15Mo3, T22 and T23, much thinner scale was observed in T91 due to higher Cr content. Nevertheless, the scales showed poor adherence to the substrate.
3. Similar degradation rate was found under deposit D2 and D3 due to the similar composition of both deposits. Under D3 deposit less aggressive alkali sulphates: $Na_2Ca_2(SO_4)_3$ and $K_2Ca_2(SO_4)_3$ formed. The dimensional metal loss data indicates the corrosion damage of 15Mo3, T22 and T23 was similar under D4 and D5 deposits.
4. Corrosion degradation decreased with increasing Cr content in the alloys for all six deposits. The median metal damage of the alloys showed the following ranking (most to the least damage): 15Mo3> T22> T23 >T91.

6 References

[1] International Energy Agency (IEA)-Report, *CO_2 emissions from fossil fuel combustion*, IEA Statistics, **2012**.
[2] K. Natesan, J. H. Park, *Int. J. Hydrogen Energy.* **2007**, *32*, 3689.
[3] S. Hastia, A. Aroonwilasa, A. Veawaba, *Energy Procedia.* **2013**, *37*, 2544.
[4] J. Skea, P. Ekins., M. Winskel, *Making the transition to a secure and low-carbon energy system*, Routledge, London **2009**.
[5] A. A. Khan, W. de Jong, P. J. Jansens, H. Spliethoff., *Fuel Process Technol.* **2009**, *90*, 21.
[6] J. Henry, G. Zhou, T. Ward., *Mater High Temp.* **2007**, *24*, 249.
[7] A. U. Syed, N. J. Simms, J. E. Oakey, *Fuel.* **2012**, *101*, 62.
[8] T. Hussain, A. U. Syed, N. J. Simms, *Fuel.* **2013**, *113*, 787.
[9] K. Natesan, A. Purohit, D. L. Rink, *Proc. of 17th Annual Conference on Fossil Energy Materials.* Baltimore, United States April 22–25 **2003**.
[10] T. Dudziak, T. Hussain, N. J. Simms, A. U. Syed, J. E. Oakey, *Corros. Sci.* **2014**, *79*, 184.
[11] N. J. Simms, A. T. Fry., Modelling fireside corrosion of heat exchangers in co-fired pulverised fuel power systems. In: Lecomte-Beckers J, Carton M (eds.) *Materials for advanced power engineering.* Julich: Forschungszentrum;Germany, **2010**.

[12] N. J. Simms, P. J. Kilgallon, J. E. Oakey, *Mater Sci. Eng Energy Syst.* **2007**, *2*, 154.
[13] C. W. Bale, A. D. Pelton, W. J. Thompson, G. Eriksson, K. Hack, P. Chartrand, S. Decterov, Jung, J. Melancon, S. Petersen, FactSage 6.2 (database: FACT), *Copyright Thermfact and GTT-Technologies 1976* **2010**.
[14] A. D. Smigelskas, E. O. Kirkendall, *Trans. AIME* **1947**, *171*, 130.
[15] J. Ellis, M. Haw, Chromium Carbides, *Materials World* **1997**, *5* (11), 1.
[16] P. Huczkowski, T. Olszewski, M. Schiek, B. Lutz, G. R. Holcomb, V. Shemet, W. Nowak, G. H. Meier, L. Singheiser, W. J. Quadakkers, *Mater. Corros.* **2014**, *65*, 2.
[17] J. Stringer, I. G. Wright, *Oxi. Met.* **1995**, *44*, 265.
[18] A. Syed, *PhD Thesis*, Cranfield University, Cranfield, United Kingdom **2011**.
[19] S. Kihara, T. Isozaki, A. Ohtomo, *Proc. JIMIS–3 High-Temperature Corrosion*, Tokyo, Japan **1983**.
[20] A. Karlsson, P. J. Møller, V. Johansen, *Corros. Sci.* **1990**, *30*, 153.
[21] F. Mansfeld, U. Bertocci, *Electrochemical Corrosion Testing, ASTM International*, Baltimore **1981**.
[22] K. Natesan, *J. Met.* **1991**, *43*, 61.
[23] W. T. Reid, *External Corrosion and Deposits*, American Elsevier, New York **1971**.
[24] M. Bellotto, A. Gualtieri, G. Artioli, S. M. Clark, *Phys. Chem. Minerals.* **1995**, *22*, 207.
[25] M. Aho, J. Silvennoinen, *Fuel* **2004**, *84*, 1299.
[26] P. Viklund, *PhD Thesis*, KTH, Stockholm, Sweden **2011**.
[27] U. Nieken, O. Watzenburger, *Chem. Eng. Sci.* **1999**, *54*, 2619.
[28] E. Reese, H. J. Grabke, *Mater. Corros.* **1992**, *43*, 547.
[29] E. Reese, H. J. Grabke, *Mater. Corros.* **1993**, *44*, 41.

(Received: July 4, 2014) W7886
(Accepted: December 2, 2014)

